THE JOURNAL OF PHYSICAL CHEMISTRY C
A JOURNAL OF THE AMERICAN CHEMICAL SOCIETY

pubs.acs.org/JPCC

Article

Probing Interfacial Halogen-Bonding Effects with Halogenated Organic Dyes and a Lewis Base-Decorated Transition Metal-Based Redox Shuttle at a Metal Oxide Interface in Dye-Sensitized Solar Cells

Christine Curiac,[⊥] Leigh Anna Hunt,[⊥] Md Abdus Sabuj,[⊥] Qing Li, Alexandra Baumann, Hammad Cheema, Yanbing Zhang, Neeraj Rai,* Nathan I. Hammer,* and Jared H. Delcamp*

Cite This: *J. Phys. Chem. C* 2021, 125, 17647−17659

Read Online

ACCESS | Metrics & More | Article Recommendations | Supporting Information

ABSTRACT: Metal-free bis-cyclopentadithiophene-based molecular sensitizers with varying halogens (Cl, Br, and I) installed at a terminal position in conjugation with the dye frontier molecular orbital π-system are studied in combination with two cobalt redox shuttles (RSs): with and without a nonmetal-coordinated nitrogen atom (pyrazine or pyridine) accessible to the halide-decorated dyes. This systematic study employs UV−vis absorption, cyclic voltammetry, density functional theory calculations, and nanosecond transient absorption spectroscopy to probe the influence of possible halogen-bonding between the dyes and the pyrazine-based RS on electron-transfer reactions and effects on dye-sensitized solar cell performances. The results of this study imply a possible halogen-bonding event occurring between the halogenated dyes and the halogen binding RS with substantial effects on electron-transfer reaction rates.

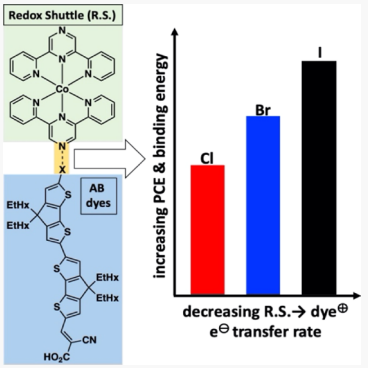

INTRODUCTION

Photoinduced electron-transfer systems with molecular organic dyes at interfaces are critically important to numerous applications including dye-sensitized photoelectrochemical cells,[1−5] dye-sensitized solar cells (DSCs),[6−14] and solar redox batteries.[15−22] Metal oxide semiconductor (*e.g.*, TiO_2)-bound chromophore devices are common in the literature and typically rely on a photoinduced charge-transfer (CT) event from the dye to the metal oxide followed by regeneration to the ground state of the dye from a redox shuttle (RS). Studies on TiO_2−dye−RS systems with preorganized transiently stable noncovalent interactions between the dye and RS could lead to improved electron-transfer reaction kinetics and improve device performances. Ideally, the dye−RS noncovalent bond could be used to increase the effective concentration of the RS at the dye interface, and the noncovalent bond could also be broken allowing for diffusion of the oxidized RS from the TiO_2−dye interface.

Halogen bonds typically refer to noncovalent interactions involving a halogen atom,[23] which, to the best of our knowledge, have not yet been probed between transition metal-based RSs and a halogen on an organic dye at a metal oxide surface. The literature has shown significant precedent for the use of a Lewis base or halogen functionality on dyes coordinating to X_2 and X^- groups in solution[23,24] and at surfaces.[25−30] Expanding from X^- coordination to transition metal-based RSs with Lewis base functionality coordination could modulate electron-transfer kinetics with these systems. Designing systems with faster electron regeneration kinetics using transition metal-based RSs via self-assembly through noncovalent interactions is therefore an intriguing direction.[31−33] This study employs an RS with an accessible peripheral Lewis base site Co(*N*-tpy)$_2$, where *N*-tpy is 2,6-di(pyrid-2-yl)pyrazine, targeted for studies with a series of organic dyes having a single atom change (Cl, Br, and I) at a TiO_2 semiconductor interface (Figure 1).

The target dyes use electron-rich cyclopentadithiophene (CPDT) donor groups with an attached halogen atom at one terminal position (Figure 1). A control with a hydrogen atom at the terminal position is also targeted as a comparison material for some studies. The use of two CPDT groups results in extended π-conjugation of the system which allows for both broader and increased visible light absorption past the absorption of the RSs to enable the spectroscopic monitoring of the dye during electron-transfer reactions (*vide infra*).[34] The use of thiophene-based donors provides an opportunity to

Received: June 9, 2021
Revised: July 27, 2021
Published: August 9, 2021

https://doi.org/10.1021/acs.jpcc.1c05051
J. Phys. Chem. C 2021, 125, 17647−17659

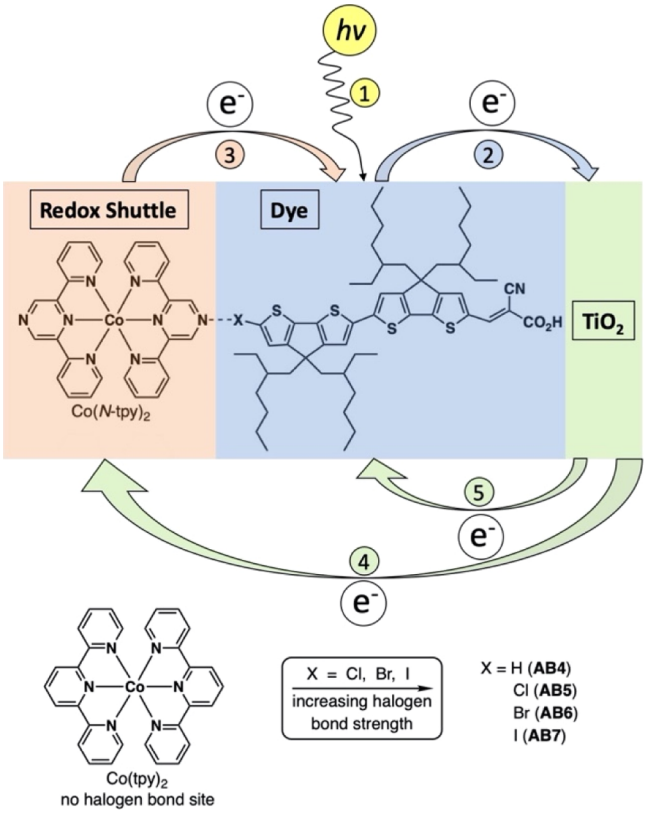

Figure 1. Noncovalent interaction between a cobalt-based RS (Co(*N*-tpy)$_2$) and a halogen atom on a dye being interrogated in this study.

examine the effects of having a halogen in conjugation with an intramolecular charge-transfer (ICT) π-system when an acceptor group is placed at the opposite terminal to the halide. The cyanoacrylic acid (CAA) group is used as a TiO_2-anchoring acceptor known to undergo facile electron injection into TiO_2.[35,36] Positive charge buildup near the halide after electron transfer from a dye to TiO_2 is likely with this molecular design.[37] Positive charge buildup has been shown to increase halogen-bond donor strength resulting in a stronger halogen bond for more dramatic effects.[38] This molecular engineered construct exposes the halogen to the environment above the TiO_2 film surface functionalized with the dye. A Lewis base-decorated transition metal-based RS in solution can then be used to probe halogen-bonding effects at the TiO_2–dye-X surface experimentally and computationally. As a control, a transition metal-based RS without a Lewis base-decorated periphery is also examined in this system.

Several electron-transfer reactions can occur upon photoexcitation of the dye under open-circuit conditions using the TiO_2–dye-X–RS system, including (1, ICT) the photoexcitation of the dye bound to the surface of TiO_2 to promote an ICT event, (2, injection) electron injection into the TiO_2 conduction band (CB) yielding a dye cationic species, (3, regeneration) an electron transfer to an oxidized dye by a reduced RS in solution, (4, recombination) an electron transfer back to the oxidized RS from the TiO_2 CB, and (5, back electron transfer [BET]) an electron transfer from the TiO_2 CB to an oxidized dye molecule. Arrows 1–3 represent productive electron-transfer reactions, while arrows 4–5 represent nonproductive electron-transfer reaction pathways. The arrows in Figures 1 and 2 correspond to the numbers listed.

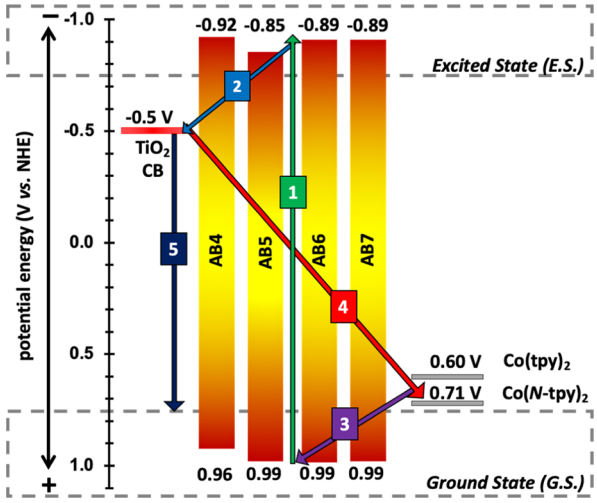

Figure 2. Energy-level diagram illustrating electron-transfer reaction pathways between the dyes **AB4**–**AB7**, the TiO_2 CB, and the RSs used in this study.

A halogen-bonded dye–RS system could have a significant impact on the electron-transfer reactions indicated in arrows 3–5. Arrow 3 (or regeneration) in this scheme is particularly important to photoelectrochemical cells, solar cells, solar batteries, and dye-sensitized photodetectors since a competitive parasitic pathway, arrow 5 or BET, exists for the transfer of electrons from the TiO_2 CB to the oxidized dye which limits the overall quantum yield of these devices. Arrows 3 and 5 are both readily monitored by transient absorption spectroscopy in the presence or absence of an RS, respectively, by the disappearance of the resulting cationic dye species. The diminishing dye cation signature over time provides a method of analyzing the potential influence of halogen-bonding on the kinetics of electron transfer when RSs with and without Lewis basic functionality are compared. Arrow 4 (recombination) can be probed with small modulated photovoltage transient (SMPVT) techniques or electrochemical impedance spectroscopy (EIS). This series of spectroscopic techniques allows for the analysis of possible halogen-bonding effects on arrows 3–5.

MATERIALS

All commercially obtained reagents were used as received. 4*H*-Cyclopenta[2,1-b:3,4-b′]dithiophene and 2-ethylhexyl bromide were purchased from Matrix Scientific. Thin-layer chromatography (TLC) was conducted with Sorbtech silica XHL TLC plates and visualized with UV. Flash silica gel column chromatography was performed with Sorbtech P60, 40–63 μm (230–400 mesh). ^{1}H and ^{13}C NMR spectra were recorded on Bruker Avance-300 (300 MHz), Bruker Avance-400 (400 MHz), and Bruker Avance-500 (500 MHz) spectrometers and are reported in ppm using a solvent as an internal standard ($CDCl_3$ at 7.26 ppm and CD_3CN at 1.94 ppm). Data are reported as s = singlet, d = doublet, t = triplet, q = quartet, p = pentet, m = multiplet, br = broad, ap = apparent, and dd = doublet of doublets; coupling constant(s) in Hz. UV spectra were measured with a Cary 5000 UV–vis–NIR spectrometer. Cyclic voltammetry (CV) curves were measured with a CH Instruments electrochemical analyzer CHI600E. 0.1 M tetrabutylammonium hexafluorophosphate was used as the electrolyte. The working electrode is glassy carbon, the reference electrode is a silver wire, and the counter

https://doi.org/10.1021/acs.jpcc.1c05051
J. Phys. Chem. C 2021, 125, 17647–17659

Scheme 1. Synthetic Route for Target Dyes AB4, AB5, AB6, and AB7

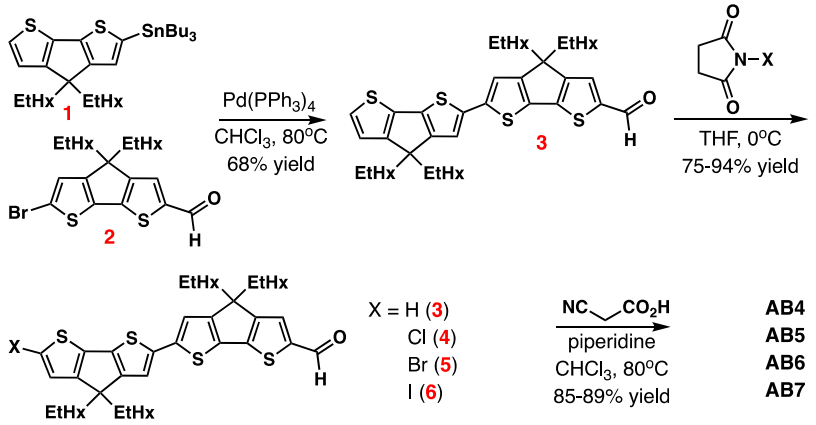

Scheme 2. Synthetic Route to $[Co(N\text{-tpy})_2][TFSI]_2$ and $[Co(N\text{-tpy})_2][TFSI]_3$

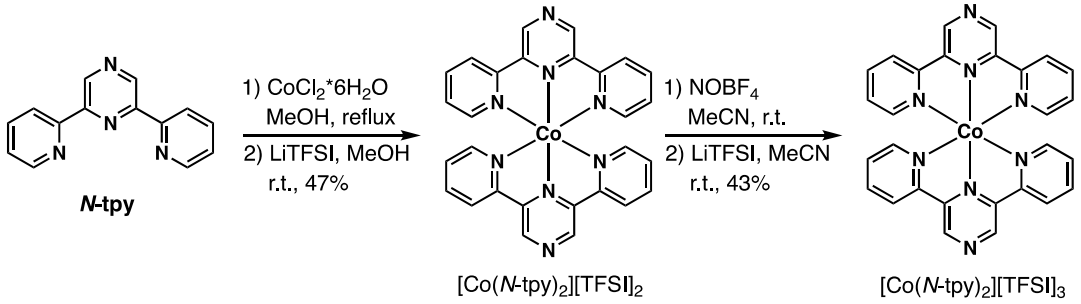

electrode is platinum with a scan rate of 100 mV/s. Ferrocene is used as an internal standard (taken as 0.64 V *vs* normal hydrogen electrode (NHE) in MeCN; 0.70 V *vs* NHE in DCM) and decamethylferrocene (taken as 0.05 V *vs* NHE in MeCN) was used as an internal standard for $Co(N\text{-tpy})_2$ due to overlap of signals with ferrocene.[39,40]

Spectroelectrochemistry data were collected with a honeycomb spectroelectrochemical cell system (Pine Research Instrumentation) using a 1 cm × 1 cm quartz cuvette (Pine Research part RRPG094), honeycomb electrode card (Pine Research part AB01STC1PT), reference electrode (Pine Research part RRPEAGCL2), and topped off with a honeycomb cell cap (Pine Research part AC01STCCAP3). The honeycomb electrode card is composed of a ceramic substrate, platinum electrodes (working and counter), and silicon dioxide as an active area insulator. The honeycomb working electrode portion has 19 holes (0.50 mm diameter and 0.75 mm center-to-center distance). The counter electrode consists of two connected exposed metal strips above the honeycomb working electrode. Ag/AgCl is used as the reference electrode. The honeycomb electrode card connects via a mini-USB-to-banana clip generic cable (Pine Research part RRPECBL2) to a potentiostat (CH Instruments Electrochemical Analyzer CHI600E). The light source (UV/vis/NIR light source, Pine Research part RRAVSP) and spectrometer (AvaSpec-ULS2048-USB2-50 spectrometer; Pine Research part RRAVSP3) were used in conjunction to the AvaSoft8 software program to produce the absorption spectra during the oxidation of the dye.

Tributyl-(4,4-diethylhexyl-4a,7a-dihydro-4*H*-cyclopenta[2,1-b; 3,4-b′]dithiophen-2-yl)-stannane (**1**),[34,41] 6′-bromo-4,4-diethylhexyl-4*H*-cyclopenta[2,1-b:3,4-b′]dithiophene-2-carbaldehyde (**2**),[42] $[Co(tpy)_2][TSFI]_2$,[43] $[Co(tpy)_2][TSFI]_3$,[43] and 2,6-di(pyrid-2-yl)pyrazine (*N*-tpy)[44] are previously reported (see Schemes 1 and 2 for numbering and naming). Analogues of the following compounds are reported with hexyl chains in place of the ethylhexyl chains with slightly modified synthetic procedures used below: 4,4,4′,4′-tetraethylhexyl-4a,7a,4′,7′b-tetrahydro-4*H*,3′a*H*-[2,2′]bi[cyclopenta[2,1-b; 3,4-b′]-dithiophenyl]-6-carbaldehyde (**3**),[34] 6′-bromo-4,4,4′,4′-tetraethylhexyl-4a,7a,4′,7′b-tetrahydro-4*H*,3′a*H*-[2,2′]bi[cyclopenta-[2,1-b; 3,4-b′]dithiophenyl]-6-carbaldehyde (**5**),[34] and 2-cyano-3-(4,4,4′,4′-tetraethylhexyl-4a,7a,4′,7′b-tetrahydro-4*H*,3′a*H*-[2,2′]bi[cyclopenta[2,1-b; 3,4-b′]dithiophenyl]-6-yl)-acrylic acid (**AB4**).[34] ^{13}C NMR data are reported for **3**−**6** and **AB4**−**AB7** despite being a mixture of multiple diastereomers due to the four ethylhexyl chains having stereocenters which causes a number of the carbon atoms to have unique shifts depending on the diastereomer which complicates the ^{13}C NMR spectrum.

SYNTHESIS

4,4,4′,4′-Tetraethylhexyl-4a,7a,4′,7′b-tetrahydro-4*H*,3′a*H*-[2,2′]bi[cyclopenta[2,1-b; 3,4-b′]dithiophenyl]-6-carbaldehyde (3). In a 100 mL round-bottom flask, 6′-bromo-4,4-diethylhexyl-4*H*-cyclopenta[2,1-b:3,4-b′]-dithiophene-2-carbaldehyde (**2**)[42] (0.528 g, 1.04 mmol) and tributyl-(4,4-diethylhexyl-4a,7a-dihydro-4*H*-cyclopenta[2,1-b; 3,4-b′]dithiophen-2-yl)-stannane (**1**)[34,41] (0.663 g, 1.04 mmol) were dissolved in chloroform (31 mL). The solution was then degassed for about 30 min with N_2 and $Pd(PPh_3)_4$ (0.120 g, 0.104 mmol) was added. The solution was sealed in a pressure flask and heated to 80 °C until completion. The mixture was then extracted with dichloromethane (DCM) and water and then dried with sodium sulfate. The crude product **3** was purified with silica gel chromatography with 25% DCM/

https://doi.org/10.1021/acs.jpcc.1c05051
J. Phys. Chem. C 2021, 125, 17647−17659

hexanes to give pure **3** (0.588 g, 68%). ^{1}H NMR (400 MHz, $CDCl_3$): δ 9.82 (s, 1H), 7.57−7.52 (m, 1H), 7.17 (ap d, J = 4.8 Hz, 1H), 7.08−7.06 (m, 1H), 7.02 (m, 1H), 6.95−6.93 (m, 1H), 2.00−1.80 (m, 8H), 1.20−0.50 (m, 60H) ppm. ^{13}C NMR (400 MHz, $CDCl_3$): δ 182.5, 163.1, 158.5, 157.3, 143.2, 142.7, 137.0, 136.6, 136.6, 130.8, 125.3, 122.5, 119.3, 119.2, 119.1, 117.7, 117.6, 54.2, 53.9, 43.2, 35.4, 35.2, 34.3, 28.7, 27.7, 27.4, 22.9, 14.2, 10.9, 10.7 ppm. HRMS (ESI positive mode) m/z calc'd for $C_{51}H_{74}OS_4$ $[M]^+$: calculated 830.4622, found 830.4615.

6′-Chloro-4,4,4′,4′-tetraethylhexyl-4a,7a,4′,7′b-tetrahydro-4*H*,3′a*H*-[2,2′]bi[cyclopenta[2,1-b; 3,4-b′]dithiophenyl]-6-carbaldehyde (4). In a 10 mL round-bottom flask, 4,4,4′,4′-tetraethylhexyl-4a,7a,4′,7′b-tetrahydro-4*H*,3′a*H*-[2,2′]bi[cyclopenta[2,1-b; 3,4- b′]dithiophenyl]-6-carbaldehyde (**3**) (0.100 g, 0.120 mmol) was dissolved in 2.9 mL of tetrahydrofuran. The solution was then degassed for about 10 min with N_2 and cooled to 0 °C. Recrystallized *N*-chlorosuccinimide (0.018 g, 0.132 mmol) was then added. The reaction mixture was kept under N_2, stirred at 0 °C for 1 h, and then allowed to warm to room temperature for 16 h. The mixture was then extracted with diethyl ether and water and dried with sodium sulfate. The crude product **4** was purified with silica gel chromatography with 25% DCM/hexanes to give pure **4** (0.102 g, 98%). ^{1}H NMR (400 MHz, $CDCl_3$): δ 9.86−9.81 (m, 1H), 7.60−7.53 (m, 1H), 7.11−6.97 (m, 2H), 6.84 (ap t, J = 3.8 Hz, 1H), 2.01−1.77 (m, 8H), 1.14−0.51 (m, 60H) ppm. ^{13}C NMR (400 MHz, $CDCl_3$): δ 182.6, 163.0, 157.5, 157.3, 155.5, 148.1, 142.9, 142.8, 137.1, 136.3, 134.1, 130.8, 129.3, 129.2, 122.1, 119.0, 117.9, 54.9, 54.2, 43.1, 35.4, 35.3, 34.4, 34.2, 29.9, 28.7, 28.6, 27.7, 27.6, 27.5, 27.5, 27.4, 22.9, 14.2, 10.9, 10.7 ppm. ESI HRMS m/z: $[M + Cs]^+$ calcd for $C_{51}H_{73}ClOS_4Cs$, 997.3287, found, 997.3277.

6′-Bromo-4,4,4′,4′-tetraethylhexyl-4a,7a,4′,7′b-tetrahydro-4*H*,3′a*H*-[2,2′]bi[cyclopenta[2,1-b; 3,4-b′]dithiophenyl]-6-carbaldehyde (5). In a 10 mL round-bottom flask, 4,4,4′,4′-tetraethylhexyl-4a,7a,4′,7′b-tetrahydro-4*H*,3′a*H*-[2,2′]bi[cyclopenta[2,1-b; 3,4-b′]dithiophenyl]-6-carbaldehyde (**3**) (0.100 g, 0.120 mmol) was dissolved in 2.9 mL of tetrahydrofuran. The solution was then degassed for about 10 min with N_2 and cooled to 0 °C. Recrystallized NBS (*N*-bromosuccinimide, 0.024 g, 0.132 mmol) was then added. The reaction mixture was kept under N_2, stirred at 0 °C for 1 h, and then allowed to warm to room temperature for 16 h. The mixture was then extracted with diethyl ether and water and dried with sodium sulfate. The crude product **5** was purified with silica gel chromatography with 25% DCM/hexanes to give **5** (0.109 g, 91%). ^{1}H NMR (400 MHz, $CDCl_3$): δ 9.82 (s, 1H), 7.55 (ap t, J = 3.7 Hz, 1H), 7.08−7.00 (m, 2H), 6.96 (ap t, J = 4.1 Hz, 1H), 2.02−1.76 (m, 8H), 1.19−0.41 (m, 60H) ppm. ^{13}C NMR (400 MHz, $CDCl_3$): δ 182.6, 163.1, 157.7, 157.2, 156.7, 148.1, 142.9, 142.8, 137.2, 137.0, 136.3, 134.1, 130.8, 125.5, 119.0, 117.8, 111.4, 54.7, 54.2, 43.1, 35.3, 34.4, 34.3, 34.2, 28.7, 28.6, 27.7, 27.6, 27.5, 27.4, 22.9, 22.9, 22.9, 14.2, 10.9, 10.8, 10.7 ppm. HRMS (ESI positive mode) m/z: $[M + Cs]^+$ calcd for $C_{51}H_{73}BrOS_4Cs$, 1041.2782; found, 1041.2772.

6′-Iodo-4,4,4′,4′-tetraethylhexyl-4a,7a,4′,7′b-tetrahydro-4*H*,3′a*H*-[2,2′]bi[cyclopenta[2,1-b; 3,4-b′]dithiophenyl]-6-carbaldehyde (6). In a 10 mL round-bottom flask, 4,4,4′,4′-tetraethylhexyl-4a,7a,4′,7′b-tetrahydro-4*H*,3′a*H*-[2,2′]bi[cyclopenta[2,1-b; 3,4-b′]dithiophenyl]-6-carbaldehyde (**3**) (0.050 g, 0.060 mmol) was dissolved in 1.4 mL of tetrahydrofuran. The solution was then degassed for about 10 min with N_2 and cooled to 0 °C. Recrystallized *N*-iodosuccinimide (0.015 g, 0.066 mmol) was then added. The reaction mixture was kept under N_2, stirred at 0 °C for 1 h, and then allowed to warm to room temperature for 16 h. The mixture was then extracted with diethyl ether and water and dried with sodium sulfate. The crude product **6** was purified with silica gel chromatography with 25% DCM/hexanes to give pure **6** (0.034 g, 60%). ^{1}H NMR (400 MHz, $CDCl_3$): δ 9.82 (s, 1H), 7.55 (ap t, J = 4.0 Hz, 1H), 7.12 (ap t, J = 4.1 Hz, 1H), 7.09−6.98 (m, 2H), 2.12−1.69 (m, 8H), 1.16−0.18 (m, 60H) ppm. ^{13}C NMR (400 MHz, $CDCl_3$): δ 182.6, 163.1, 158.6, 158.2, 158.1, 157.4, 148.1, 142.9, 142.7, 141.7, 137.3, 136.2, 134.2, 131.9, 130.8, 129.3, 119.1, 119.0, 118.0, 117.9, 71.9, 71.8, 54.2, 53.9, 43.17, 43.1, 35.3, 34.5, 34.4, 34.2 39.8, 28.7, 28.6, 27.8, 27.7, 27.6, 27.5, 27.4, 27.3, 22.9, 14.3, 14.2, 10.9, 10.8, 10.7 ppm. ESI HRMS m/z: $[M + Cs]^+$ calcd for $C_{51}H_{73}IOS_4Cs$, 1089.2643; found 1089.2625.

2-Cyano-3-(4,4,4′,4′-tetraethylhexyl-4a,7a,4′,7′b-tetrahydro-4*H*,3′a*H*-[2,2′]bi[cyclopenta[2,1-b; 3,4-b′]dithiophenyl])-acrylic Acid (AB4). In an 8.0 mL vial, 4,4,4′,4′-tetraethylhexyl-4a,7a,4′,7′b-tetrahydro-4*H*,3′a*H*-[2,2′]bi[cyclopenta[2,1-b; 3,4-b′]dithiophenyl]-6-carbaldehyde (**3**) (0.100 g, 0.120 mmol) was dissolved in 2.4 mL of chloroform. The mixture was then degassed with N_2 for approximately 30 min. Cyanoacetic acid (0.031 g, 0.360 mmol) and piperidine (0.083 mL, 0.840 mmol) were added to the vial, which was then sealed with a polytetrafluoroethylene (PTFE)-coated rubber septum inside a screw cap, heated to 90 °C, and allowed to stir for 16 h. The reaction mixture was diluted with DCM and purified through a plug of silica gel with the following elution solvents sequentially: 100% DCM, then 10% methanol/DCM, and finally 12% methanol/3% acetic acid/DCM. The solvent of the third fraction was evaporated under reduced pressure. The dye (**AB4**) was then extracted with hexanes and water and purified further with a CombiFlash R_f^+ chromatography system (RediSep R_f gold high-performance silica gel, 0% methanol/DCM gradually increasing to 10% methanol/DCM) to give the final pure dye (0.070 g, 65%). ^{1}H NMR (400 MHz, $CDCl_3$): δ 8.30 (br s, 1H), 7.70−7.56 (br m, 1H), 7.20 (ap d, J = 4.9 Hz, 1H), 7.15−7.08 (m, 1H), 7.08−7.00 (m, 1H), 6.99−6.92 (m, 1H), 2.10−1.79 (m, 8H), 1.21−0.54 (m, 60H) ppm. HRMS (ESI negative mode) m/z: $[M]^-$ calcd for $C_{54}H_{75}NO_2S_4$, 897.4681; found, 897.4676.

2-Cyano-3-(6′-chloro-4,4,4′,4′-tetraethylhexyl-4a,7a,4′,7′b-tetrahydro-4*H*,3′a*H*-[2,2′]bi[cyclopenta-[2,1-b; 3,4-b′]dithiophenyl])-acrylic Acid (AB5). In an 8.0 mL vial, 6′-chloro-4,4,4′,4′-tetraethylhexyl-4a,7a,4′,7′b-tetrahydro-4*H*,3′a*H*-[2,2′]bi[cyclopenta[2,1-b; 3,4-b′]dithiophenyl])-6-carbaldehyde (**4**) (0.05 g, 0.058 mmol) was dissolved in 1.2 mL of chloroform. The mixture was then degassed with N_2 for approximately 30 min. Cyanoacetic acid (0.015 g, 0.173 mmol) and piperidine (0.040 mL, 0.406 mmol) were added to the vial, which was then sealed with a PTFE-coated rubber septum inside a screw cap, heated to 90 °C, and allowed to stir for 16 h. The reaction mixture was diluted with DCM and purified through a plug of silica gel with the following solvents sequentially: 100% DCM, then 10% methanol/DCM, and finally 12% methanol/3% acetic acid/DCM. The solvent of the third fraction was evaporated under reduced pressure. The dye (**AB5**) was then extracted with hexanes and water and purified further with a CombiFlash R_f^+ chromatography system (RediSep R_f gold high-performance silica gel, 0% methanol/

https://doi.org/10.1021/acs.jpcc.1c05051
J. Phys. Chem. C 2021, 125, 17647−17659

DCM gradually increasing to 10% methanol/DCM) to give the final pure dye (0.050 g, 92%). ^{1}H NMR (400 MHz, $CDCl_3$): δ 8.30 (s, 1H), 7.71−7.54 (br m, 1H), 7.09 (br s, 1H), 7.03 (br s, 1H), 6.85 (br s, 1H), 2.12−1.74 (m, 8H), 1.20−0.40 (m, 60H ppm. IR (neat) ν = 3340, 2944, 2923, 2854, 2333, 2114, 1602, 1593 cm^{-1}. ESI HRMS m/z: $[M - H]^-$ calcd for $C_{54}H_{73}ClNO_2S_4$, 930.4213; found, 930.4236.

2-Cyano-3-(6′-bromo-4,4,4′,4′-tetraethylhexyl-4a,7a,4′,7′b-tetrahydro-4*H*,3′a*H*-[2,2′]bi[cyclopenta-[2,1-b; 3,4-b′]dithiophenyl])-acrylic Acid (AB6). In an 8.0 mL vial, 6′-bromo-4,4,4′,4′-tetraethylhexyl-4a,7a,4′,7′b-tetrahydro-4*H*,3′a*H*-[2,2′]bi[cyclopenta[2,1-b; 3,4-b′]-dithiophenyl]-6-carbaldehyde (**5**) (0.05 g, 0.055 mmol) was dissolved in 1.1 mL of chloroform. The mixture was then degassed with N_2 for approximately 30 min. Cyanoacetic acid (0.014 g, 0.165 mmol) and piperidine (0.038 mL, 0.385 mmol) were added to the vial, which was then sealed with a PTFE-coated rubber septum inside a screw cap, heated to 90 °C, and allowed to stir for 16 h. The reaction mixture was diluted with DCM and purified through a plug of silica gel with the following solvents sequentially: 100% DCM, then 10% methanol/DCM, and finally 12% methanol/3% acetic acid/DCM. The solvent of the third fraction was evaporated under reduced pressure. The dye (**AB6**) was then extracted with hexanes and water and purified further with a CombiFlash R_f^+ chromatography system (RediSep R_f Gold high-performance silica gel, 0% methanol/DCM gradually increasing to 10% methanol/DCM) to give the final pure dye (0.05 g, 95%). ^{1}H NMR (300 MHz, $CDCl_3$): δ 8.30 (s, 1H), 7.70−7.55 (br m, 1H), 7.09 (s, 1H), 7.03 (s, 1H), 6.97 (ap t, J = 3.1 Hz, 1H), 2.10−1.76 (m, 8H), 1.17−0.49 (m, 60H) ppm. IR (neat) ν = 3340, 2944, 2923, 2854, 2333, 2114, 1602, 1593 cm^{-1}. ESI HRMS m/z: $[M + Cs]^+$ calcd for $C_{54}H_{74}BrNO_2S_4Cs$, 1108.2840; found, 1108.2832.

2-Cyano-3-(6′-iodo-4,4,4′,4′-tetraethylhexyl-4a,7a,4′,7′b-tetrahydro-4*H*,3′a*H*-[2,2′]bi[cyclopenta-[2,1-b; 3,4-b′]dithiophenyl])-acrylic Acid (AB7). In an 8.0 mL vial, 6′-iodo-4,4,4′,4′-tetraethylhexyl-4a,7a,4′,7′b-tetrahydro-4*H*,3′a*H*-[2,2′]bi[cyclopenta[2,1-b; 3,4-b′]dithiophenyl]-6-carbaldehyde (**6**) (0.0173 g, 0.0181 mmol) was dissolved in 0.4 mL of chloroform. The mixture was then degassed with N_2 for approximately 30 min. Cyanoacetic acid (0.005 g, 0.0542 mmol) and piperidine (0.013 mL, 0.127 mmol) were added to the vial, which was then sealed with a PTFE-coated rubber septum inside a screw cap, heated to 90 °C, and allowed to stir for 16 h. The reaction mixture was diluted with DCM and purified through a plug of silica gel with the following solvents sequentially: 100% DCM, then 10% methanol/DCM, and finally 12% methanol/3% acetic acid/DCM. The solvent of the third fraction was evaporated under reduced pressure. The dye (**AB7**) was then extracted with hexanes and water and purified further with a CombiFlash R_f^+ chromatography system (RediSep R_f gold high-performance silica gel, 0% methanol/DCM gradually increasing to 10% methanol/DCM) to give the final pure dye (0.017 g, 90%). ^{1}H NMR (400 MHz, $CDCl_3$): δ 8.29 (br s, 1H), 7.70−7.55 (br m, 1H), 7.13 (ap t, J = 4.1 Hz, 1H), 7.09 (br s, 1H), 7.03 (br s, 1H), 1.93−1.87 (m, 8H), 1.16−0.49 (m, 60H) ppm. IR (neat) ν = 3340, 2944, 2923, 2854, 2333, 2114, 1602, 1593 cm^{-1}. ESI HRMS m/z: $[M + Cs]^+$ calcd for $C_{54}H_{74}INO_2S_4Cs$, 1156.2702; found, 1156.2683.

[Co(*N*-tpy)$_2$][TSFI]$_2$. In a 1000 mL round-bottom flask, $CoCl_2 \cdot 6H_2O$ (2.47 g, 10.4 mmol) was stirred in 520 mL of methanol until completely dissolved. *N*-tpy (4.85 g, 20.7 mmol) was then added to the solution and the reaction mixture was sealed and refluxed for 16 h. The solution was then cooled to room temperature. LiTSFI (6.12 g, 20.7 mmol) was dissolved in minimal methanol and then added to the solution and stirred for 1 h. Half of the solvent was removed under reduced pressure, and water was added until a precipitate formed. The solution was filtered and washed with a methanol/water solution to obtain the final product as dark red powder (4.16 g, 47% yield). ^{1}H NMR (400 MHz, $CDCl_3$): δ 90.67 (br s, 1H), 49.66 (s, 1H), 34.14 (s, 1H), 30.43 (s, 1H), 10.39 (s, 1H) ppm. ^{19}F NMR (400 MHz, $CDCl_3$): δ 80.2 ppm. IR (neat) ν = 3088, 1601 cm^{-1}. MS (MALDI): calcd for $C_{30}H_{20}CoN_9O_4S_2F_6$ $[M - 2TFSI]^+$ 807.0, found: 807.1. CHN elemental analysis (EA) calculated for $C_{32}H_{20}CoF_{12}N_{10}O_8S_4$: C, 35.34%; H, 1.85%; N, 12.88%. Found: C, 35.41%; H, 1.72%; N, 12.90%.

[Co(*N*-tpy)$_2$][TSFI]$_3$. In a 100 mL round-bottom flask, $[Co(N\text{-tpy})_2][TSFI]_2$ (1.05 g, 1.23 mmol) was stirred in 31 mL of acetonitrile until completely dissolved. The solution was then bubbled with N_2 for 10 min. $NOBF_4$ (0.160 g, 1.35 mmol) was then added to the solution, and the reaction mixture was kept under N_2 and stirred at room temperature for 1 h. LiTSFI (0.80 g, 1.35 mmol) was dissolved in minimal acetonitrile and then added to the solution and stirred for 1 h. Half of the solvent was removed under reduced pressure, and water was added until a precipitate formed. The remaining solution was filtered and washed with water to obtain the final product as yellow powder (0.60 g, 43% yield). ^{1}H NMR (400 MHz, $CDCl_3$): δ 10.19 (s, 1H), 8.71 (dd, J = 8.0 Hz, 1.6 Hz, 1H), 8.30 (dt, J = 8.0 Hz, 1.6 Hz, 1H), 7.48 (dt, J = 5.6 Hz, 1.2 Hz, 1H), 7.31 (dd, J = 5.6 Hz, J = 1.2 Hz, 1H) ppm. ^{13}C NMR (400 MHz, $CDCl_3$): δ 155.0, 154.5, 151.6, 148.7, 144.6, 132.7, 129.4 ppm. ^{19}F NMR (400 MHz, $CDCl_3$): δ 80.25 (s) ppm. IR (neat) ν = 3117, 1607 cm^{-1}. HRMS (ESI positive mode): calcd for $C_{28}H_{20}CoN_8$ $[M - 3TFSI]^+$ 527.1143, found: 527.1115. MS (MALDI): calcd for $C_{30}H_{20}CoN_9O_4S_2F_6$ $[M - 2TFSI]^+$ 807.0, found: 807.1. CHN EA calcd for $C_{34}H_{20}CoF_{18}N_{11}O_{12}S_6$: C, 29.85%; H, 1.47%; N, 11.26%. Found: C, 29.86%; H, 1.31%; N, 11.08%.

COMPUTATIONAL METHODOLOGY

The geometry optimizations, binding energy, and time-dependent density functional theory (TDDFT) calculations were performed with the Gaussian 16 program package.[45] To account for the long-range interactions, the ωB97XD[46] functional was used with D2 dispersion corrections.[47] The residual force and density matrix were converged with tight convergence criteria, and ultrafine grid was used for the numerical integration. LANL2TZ(f) and LANL2DZdp basis sets with effective core potential[48,49] were used for the cobalt (Co) and halogens, respectively. For all other atoms, the 6-31G(d, p) basis set was used.[50] The geometry optimizations and binding energy calculations were performed with two different charge states of the dyes: neutral and oxidized states. Sample calculations on the Co(*N*-tpy)$_2$ RS with both 2+ and 3+ charges on the Co, varying the multiplicity of the system, were performed. The lowest energy state of the 3+ charge (multiplicity: 1) is 279 kcal/mol higher than the 2+ charge (multiplicity: 4). Therefore, all the calculations are performed with 2+ charge and 4 multiplicity on the RS due to practical computational considerations. First, the dyes and the cobalt complex were optimized separately, and the optimized

https://doi.org/10.1021/acs.jpcc.1c05051
J. Phys. Chem. C 2021, 125, 17647−17659

geometries were placed together for the final optimization. All the geometry optimization and binding energy calculations were performed with +2 charge on the cobalt complex and for the charged dyes, the total charge of the system was +3. For a difficult convergence case where the self-consistent field (SCF) cycles were not converged within 200 cycles, a quadratically convergence procedure[51] for SCF was utilized. Integral equation formalism of the polarizable continuum model[52−54] was used with acetonitrile as the implicit solvent. A fragment guess calculation was used to generate the initial guess for the individual fragments with a full geometry optimization afterward. To reduce the computational cost, the $-C_6H_{13}$ group was replaced with $-C_2H_5$ and all geometries were considered optimized once the forces on all atoms were converged to zero.[55] Geometry optimizations were performed without any symmetry constraint. Frequency calculations were performed on each geometry to confirm the local minima.

The analysis of binding energies (E_{BE}) involved the energy difference between the dye−cobalt complex (E_{total}) with energy of the dye ($E_{fragment\text{-}1}$) and cobalt complex ($E_{fragment\text{-}2}$). For the $E_{fragment\text{-}1}$ and $E_{fragment\text{-}2}$ energy, a single-point energy calculation was performed on the total system (cobalt complex + dyes) by replacing the other fragments with a ghost atom.

$$E_{BE} = E_{total} - E_{fragment\text{-}1} - E_{fragment\text{-}2} \quad (1)$$

For the excited states, TDDFT[56,57] calculation was performed with Tamm−Dancoff approximation.[55] The vertical excitation of the lowest 25 singlet excited states was calculated to determine key transitions in the complex. TDDFT calculations were performed at the same level of theory and basis set as density functional theory (DFT) calculations using acetonitrile as an implicit solvent.

TAS Measurements. Time-resolved absorption spectra were collected using an Edinburgh LP980 optical system. Excitation (532 nm) light was generated from a pulsed Nd:YAG laser (Continuum, Surelite II) equipped with a doubling crystal (<3 mJ/pulse; ∼1 ns pulse width) and probed with a 150 W pulsed xenon arc lamp. Time-resolved absorption decays were collected at a single wavelength of 720 nm by the use of a Czerny−Turner monochromator and photomultiplier tube and averaged over 300 laser shots. The ΔOD versus t curve is typically modeled using a Kohlrausch−Williams−Watts (KWW)[58−61] stretched exponential decay function

$$\Delta OD(t) = \Delta OD_{t=0}\, e^{-\left(\frac{t}{\tau_{KWW}}\right)^{\beta}} \quad (2)$$

where $\Delta OD_{t=0}$ represents the signal amplitude at time zero, τ_{KWW} is the stretched exponential lifetime, and β is the stretch parameter, which ranges in value from 0 to 1. The observed lifetime is calculated from the fitting parameters using a gamma function distribution of β^{-1} (eqs 3 and 4)

$$\Gamma(x) = \int_0^{\infty} u^{(x-1)}\, e^{-x}\, du \quad (3)$$

$$\tau_{obs} = \frac{\tau}{\beta}\Gamma\left(\frac{1}{\beta}\right) \quad (4)$$

The mean lifetime is then used to calculate the observed rate values obtained in the absence, k_{rec}, and presence, k_{reg}, of the redox active species (eq 5). The overall RS electron-transfer efficiency relative to BET from the TiO_2 CB is calculated using eq 6.

$$k_{obs,i} = \frac{1}{\tau_{obs,i}} \quad (5)$$

$$\phi_{reg} = \frac{k_{reg}}{k_{reg} + k_{rec}} \times 100 \quad (6)$$

We note that accurately quantifying regeneration efficiencies is challenging.[62,63] We have used a simplified equation set common in the literature which likely overestimates the regeneration efficiencies as others have noted.[64] A modified approach to these equations is presented in the Supporting Information which attempts to account for competitive electron-transfer reactions in the presence of an RS; however, we note that the values presented are only estimates with the goal of showing trends in dye behavior for this study.

nsTAS TiO_2−Dye Film Preparation. Chenodeoxycholic acid (CDCA) was purchased from Chem-Impex International. TEC 10 glass was purchased from Hartford Glass and cut into 2 × 2 cm squares, added to 0.2% Deconex 21 aqueous solution, sonicated for 10 min at room temperature, then rinsed with water, acetone, and finally ethanol. The electrodes comprised a single 5 μm mesoporous TiO_2 layer (particle size, 30 nm, Dyenamo, DN-GPS-30 TS). All the layers were screen-printed from a Sefar screen (54/137−64W). Following the print, the substrate was heated for 7 min at 125 °C and the thickness was measured with a profilometer (Alpha-Step D-500 KLA Tencor). Once the layer was deposited, the substrate was then sintered with progressive heating from 125 °C (5-min ramp from r.t., 5 min hold) to 325 °C (15 min ramp from 125 °C, 5 min hold) to 375 °C (5 min ramp from 325 °C, 5 min hold) to 450 °C (5 min ramp from 375 °C, 15 min hold) to 500 °C (5 min ramp from 450 °C, 15 min hold) using a programmable furnace (Vulcan 3-Series model 3-550). The cooled electrode was prepared by immersing the TiO_2 film into the dye solution for 3 h. The solution is 0.3 mM dye in MeCN/t-BuOH/THF mixture (1:1:1) with a 20:1 CDCA/dye mole ratio unless otherwise indicated. The electrodes were washed with acetonitrile and the dried substrates were then partially sealed with a precut semicircle of a 25 μm-thick hot melt film (Surlyn, Solaronix, "Meltonix 1170-25") and a thin glass cover slip by heating the system at 130 °C under 0.1 psi pressure for 30 s. Devices were completed by filling the cells with an electrolyte solution by injecting it into the open portion of the hot melt semicircle with a microsyringe. The electrolyte without cobalt RS (inert electrolyte) is comprised of 0.1 M LiTFSI in MeCN. The electrolyte with cobalt RS for both $Co(tpy)_2$ and $Co(N\text{-}tpy)_2$ is comprised of 0.25 M Co^{2+}, 0.05 M Co^{3+}, and 0.1 M LiTFSI in MeCN. The device is then sealed with a light-cured adhesive (Permabond UV6231) and cured under 405 nm light (390−420 nm emission base width) for 45 s with the cell active dye area shielded from light.

RESULTS AND DISCUSSION

Predicted Properties of Targeted Dyes and Synthesis. Computational studies were undertaken on all four dyes in both the neutral and cation states at the ωB97XD/6-31G(d,p) level of theory and basis set.[47−50] Analysis of the frontier molecular orbitals (MOs) indicates that the highest occupied MO (HOMO) is delocalized across the two CPDT groups for all of the neutral dyes with some HOMO contribution on the halides (Figures 3 and S26). No significant change in the HOMO position is observed based on halide choice. The

https://doi.org/10.1021/acs.jpcc.1c05051
J. Phys. Chem. C 2021, 125, 17647−17659

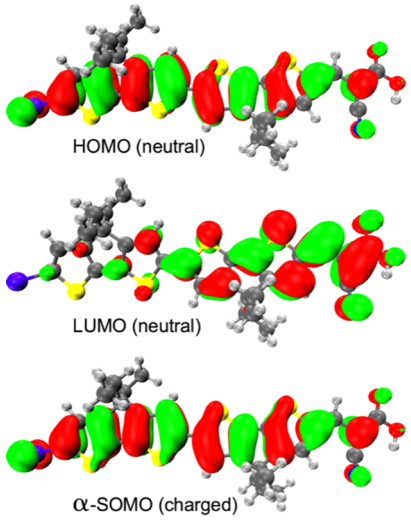

Figure 3. MO diagrams of the neutral and positively charged **AB7**. The green and red surface represents the positive and negative signs of MO at isovalue = 0.02 a.u, respectively. See Supporting Information for images of additional orbitals and **AB4**−**AB6**.

lowest unoccupied MO (LUMO) is primarily localized on the CPDT π-bridge group attached to the CAA group and the CAA acceptor. No significant change based on halide is observed for the LUMO as well. These orbitals are well-positioned spatially for efficient electron injection into the TiO_2 CB from the CAA group upon photoinduced intramolecular electron transfer from the HOMO to the LUMO.

All of the neutral dyes are behaving as ICT dyes based on the orbital positions, analysis of CT amounts, and CT distances (Table S1). Upon photoinduced electron transfer from the dye to TiO_2, a cationic dye is generated. The dye cation singly occupied MO and neutral dye HOMOs are very similar in positioning on the dyes with contributions on the halides (Figures 3 and S26). This suggests that an RS with a Lewis base functionality on the periphery could coordinate with the halide of a cationic dye for a close dye orbital interaction (Figure S28). No significant changes in free energy for electron transfers are predicted between the dyes based on orbital energies (Table S2), which allows for a direct evaluation of halogen-bonding effects.

The synthesis of the desired dyes and RSs is described in the experimental section. Briefly, the synthesis began with the Stille coupling of known stannylated CPDT **1**[34,41] and known bromo-CPDT-aldehyde **2**[42] to give bis-CPDT-aldehyde **3** in 68% yield (Scheme 1). N-halogenated succinimide electrophiles could be used to halogenate **3** to give the chloro (**4**), bromo (**5**), and iodo (**6**) derivatives in 75−94% yield. Finally, Knoevenagel condensation of aldehydes **3**−**6** with cyanoacetic acid gave the target dyes in 85−89% yield. The Lewis base-decorated RS $[Co(N\text{-tpy})_2][TFSI]_2$ was synthesized beginning from the known *N*-tpy ligand[44] by metalation with $CoCl_2 \cdot 6H_2O$ and salt metathesis with LiTFSI to give the desired product in 47% yield (Scheme 2). The oxidized RS $[Co(N\text{-tpy})_2][TFSI]_3$ was synthesized from $[Co(N\text{-tpy})_2][TFSI]_2$ by $NOBF_4$ oxidation and counter anion exchange with LiTFSI to probe halogen-bonding effects under a more practical environment with both RS oxidation states present. The RS without the peripheral Lewis base group ($[Co(tpy)_2][TFSI]_x$, where tpy is 2,2′:6′,2″-terpyridine), was synthesized in both oxidation states as described in the literature to serve as a negative control which will not halogen-bond to the dyes.[43]

Solution Measurements. The optical properties of the dyes and cobalt RSs were evaluated with steady-state absorption spectroscopy to assess the suitability of this system for nanosecond transient absorption spectroscopy (nsTAS). The dyes were found to have absorption maxima (λ_{max}) ranging from 488−503 nm with absorption curve onsets (λ_{onset}) closely grouped at 595−618 nm in DCM (Table 1, Figure 4; see Figure S23 for TiO_2 film absorption data). The λ_{max} values differ by 0.08 eV or less with higher energy values being observed as the halide increases in size. A trend is also observed for the dye molar absorptivities (ε) with a modest increase in molar absorptivity from 27,000 M^{-1} cm^{-1} to 31,000 M^{-1} cm^{-1} according to the following order: Cl < Br < I. TDDFT analysis shows similar results for the vertical transitions and oscillator strength (Table S3). The Co(*N*-tpy)$_2$ RS was found to have minimal absorption in the visible region (>400 nm) for both the Co^{2+} and Co^{3+} oxidation states in acetonitrile (MeCN), which indicates that this RS could be used for transient absorption spectroscopy (TAS) measurements with **AB4**−**AB7** (Table 1, Figure 5).

Next, the free energies for electron transfer from the RSs to the dye cations were probed by CV. The dye ground-state oxidation potentials ($E_{(S+/S)}$) were measured to be identical for the halogenated dyes at 0.99 V versus NHE (Table 1, Figures S19−S22). The RS half-wave potentials were measured at 0.60 and 0.71 V for $Co(tpy)_2^{3+/2+}$ and $Co(N\text{-tpy})_2^{3+/2+}$, respectively, which indicates a free energy for electron transfer to the dye cations from the RSs of at least 390 mV and 280 mV (Table 1, Figure 6). The dye excited-state oxidation potentials ($E_{(S+/S^*)}$) were evaluated energetically with respect to the TiO_2 CB taken at −0.5 V versus NHE. A close grouping of $E_{(S+/S^*)}$ values from −1.03 to −1.09 V is observed without correlation to the halide group. Thus, all of the dyes can inject electrons into the TiO_2 CB with favorable free energies for electron transfer by at least 530 mV.

Table 1. Optical and Electrochemical Properties of Dyes in DCM and RSs in MeCN

dye/RS	λ_{max} (nm)	ε_{max} (M^{-1} cm^{-1})	λ_{onset} (nm)[a]	$E_{(S+/S)}$ (V)	$E_{(S+/S^*)}$ (V)[b]	E_g^{opt} (eV)[a,c]
AB4	489	25000	618	0.96	−1.05	2.01
AB5	503	27000	612	0.99	−1.04	2.03
AB6	499	28000	613	0.99	−1.03	2.02
AB7	488	31000	595	0.99	−1.09	2.08
$Co(N\text{-tpy})_2^{2+}$	345	45000	375	0.71		
$Co(N\text{-tpy})_2^{3+}$	372	15000	400			

[a]Determined *via* onset program.[65] [b]Calculated according to the equation: $E_{(S+/S^*)} = E_{(S+/S)} - E_g^{opt}$. [c]Estimated from the onset of the absorption curve using the equation $E_g^{opt} = 1240/\lambda_{onset}$.

https://doi.org/10.1021/acs.jpcc.1c05051
J. Phys. Chem. C 2021, 125, 17647−17659

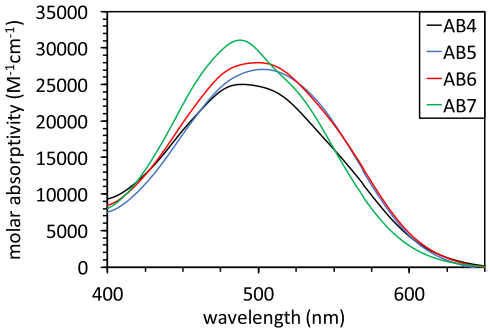

Figure 4. Molar absorptivity of dyes **AB4**−**AB7** in a DCM solution.

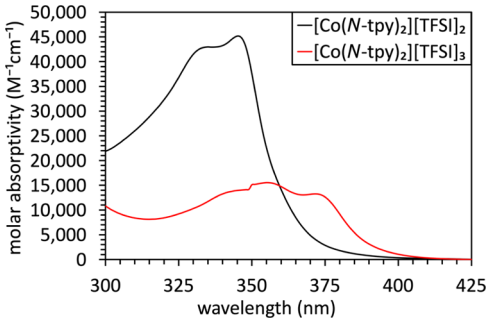

Figure 5. Molar absorptivity of RSs $[Co(N\text{-tpy})_2][TFSI]_2$ and $[Co(N\text{-tpy})_2][TFSI]_3$ in MeCN.

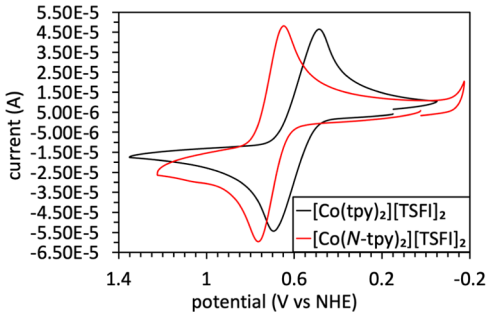

Figure 6. Cyclic voltammograms of $[Co(N\text{-tpy})_2][TSFI]_2$ and $[Co(tpy)_2][TSFI]_2$ in MeCN.

Computational Analysis. The molecular electrostatic potential (MEP) surfaces were analyzed for each of the dyes to assess the possibility of halogen-bonding to the $Co(N\text{-tpy})_2^{2+}$ RS (Figure 7). In both the neutral and cationic states of the dyes, the halide group shows a significantly positive σ-hole region. The positive potential value at the σ-hole is significantly higher for the cation than the neutral dye (0.01 vs 0.08 Hartree), which indicates a potentially stronger interaction of the Lewis basic nitrogen on $Co(N\text{-tpy})_2$ to the dye cation. The size and charge of the σ-hole increase as the halides increase in size, suggesting that $Co(N\text{-tpy})_2^{2+}$ should bind **AB7** the strongest.[28] A favorable interaction and geometry is observed computationally between the $Co(N\text{-tpy})_2^{2+}$ RS and the dye (Figures 8 and S28). The binding energy obtained from this interaction gave the following halide trend from low-to-high binding strength: Cl < Br < I with a range of −6.37 kcal/mole for **AB5** to −9.44 kcal/mole for **AB7** (Tables 2 and S4). Notably, the binding geometry of the dyes with halides differs slightly to the dye with a hydrogen atom which limits direct comparisons of **AB4** to **AB5**−**AB7**. Similar binding energies

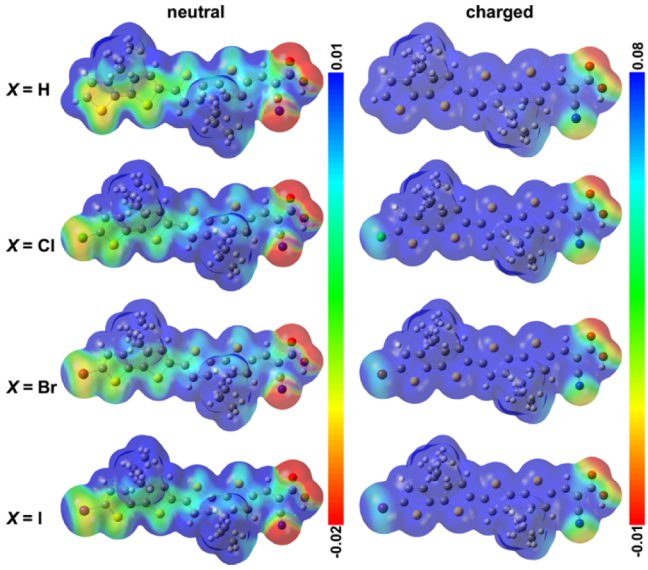

Figure 7. MEP surface for the neutral and cationic dyes. The isosurface value for the total electron density is 0.001 au with the potential value (Hartree) shown in the scales. The blue and red surface represents the highest (less electrons) and lowest (more electrons) electrostatic potential, respectively.

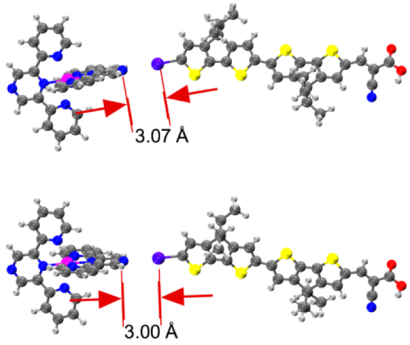

Figure 8. Optimized geometries of **AB7** with $Co(N\text{-tpy})_2$. (A) Neutral **AB7** (top) and cationic **AB7** (bottom).

Table 2. Calculated Binding Energy and Distances between the RSs and Dyes

RS	X-Dye	BE dye (kcal/mol)	BE dye$^+$ (kcal/mol)	RS-dye dist. (Å)	RS-dye$^+$ dist. (Å)
$Co(N\text{-tpy})_2^{2+}$	Cl	−6.37	−6.22	3.14	3.07
$Co(N\text{-tpy})_2^{2+}$	Br	−7.69	−7.39	3.07	3.00
$Co(N\text{-tpy})_2^{2+}$	I	−9.44	−9.30	3.07	3.00

are observed in the cationic dye states with bond distances from 3.00 to 3.07 Å, which are typical halogen-bonding distances.[23,38] The bonding distance is observed to be approximately 0.07 Å closer on average for $Co(N\text{-tpy})_2^{2+}$ to the cationic dye relative to the neutral dye. No favorable binding of the $Co(tpy)_2^{2+}$ RS to any of the neutral dyes was observed. These results suggest that a significant halogen-bonding event can take place with the dyes and $Co(N\text{-tpy})_2^{2+}$.

Surface Studies. The dyes were loaded onto TiO_2 films with similar dye loading densities of 7.33×10^{-8} to 1.37×10^{-7} mol/cm^2 as described in Supporting Information (Table S9). The dye-loading density trend follows the halide trend with **AB7** > **AB6** > **AB5**. The TiO_2-dye films were subjected to nsTAS measurements to monitor the absorption profile of the

https://doi.org/10.1021/acs.jpcc.1c05051
J. Phys. Chem. C 2021, 125, 17647−17659

dye cation on the surface of TiO_2. When measuring the kinetics on a microsecond time scale, electron transfer from the dye to the CB of TiO_2 is assumed to be completed and therefore the main signals observed are those arising from the oxidized dye. Transient decay measurements were collected to analyze the rates of the electron-transfer reaction from TiO_2 to the oxidized dye (*i.e.*, BET) and the rates of electron transfer to the oxidized dye from the RS (*i.e.*, dye regeneration). The transient cationic dye species generated is represented by an observable change in the electronic spectrum for the dyes (Figures 9 and S29−S40). The negative change in optical density (ΔOD) in the 400−575 nm region represents the disappearance of the ground-state dye species (ground-state bleaching) and the positive ΔOD in the 600−800 nm region represents absorption from the dye cation and correlates to the spectral region of the dye cation observed *via* spectroelectrochemistry in both solution and on the surface of TiO_2 (Figures S24 and S25). The dye cation absorption was monitored as a function of time at 720 nm in the absence of an RS to measure the rate of BET between 8.40×10^4 and 1.08×10^5 s^{-1} (Figures 9 and S41−S44, Table 3). Kinetic traces were fit with a stretched exponential decay function, and the corresponding rate values were calculated according to the procedure in the experimental section (Figure 10, Table 3).[58−61]

Dynamics measured with the dyes in the presence of an RS are representative of the rate of the dye neutral-state regeneration from the RS (blue and red traces) and the BET from the electron in TiO_2. The changes in decay rate when an RS is added relative to the no RS decay traces (green traces) represents faster consumption of the dye cation due to electron transfer from the RS.

All of the systems show a significant increase in the dye cation decay rate in the presence of the RS (k_{reg}) when compared to the dye cation decay rate in the absence of an RS (k_{rec}) (Tables 3 and S7). The BET reaction rates (k_{rec}) are similar ranging from 1.08×10^5 to 8.60×10^4 s^{-1} and no trend with respect to halide is observed. Upon the addition of Co(*N*-tpy)$_2^{2+}$, k_{reg} values of 3.85×10^5 to 1.82×10^5 s^{-1} are observed which track the halogen trend. As the halogen atom size increased across the dye series, the k_{reg} value decreases. This observation would be consistent with a trend expected for a halogen-bonding effect occurring between the dye cation and the RS where the halogen bond provides a spatial separation which slows electron-transfer rates between the reducing cobalt center and the dye cation. The regeneration efficiency (φ) factors in the two competing electron-transfer pathways to the dye cation *via* eq 6. φ is calculated to be 84.4, 80.0, and 68.4% for **AB5**, **AB6**, and **AB7**, respectively (see eq 6), which again shows halogen-bonding slowing the regeneration of the neutral dye.

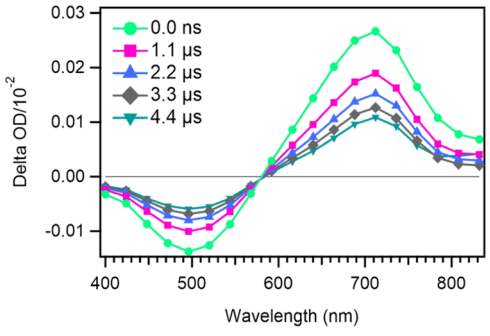

Figure 9. Transient spectrum of **AB7** on TiO_2 with 0.1 M LiTFSI in MeCN.

Table 3. Summary TAS Data for AB5, AB6, and AB7[a]

dye	k_{reg} (s^{-1})	k_{rec} (s^{-1})	φ (%)
AB5	3.85×10^5	1.08×10^5	84.4
AB6	3.45×10^5	8.60×10^4	80.0
AB7	1.82×10^5	8.40×10^4	68.4

[a]All measurements were taken under open-circuit conditions, with the pump power = <3.0 mJ/pulse and the probe wavelength set to 720 nm; The electrolyte is 0.25 M Co(*N*-tpy)$_2^{2+}$ and 0.1 M LiTFSI.

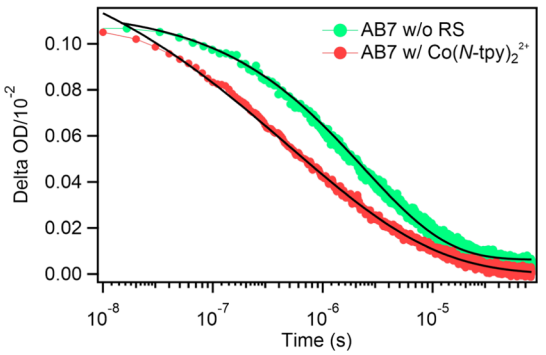

Figure 10. Decay plots resulting from TAS for **AB7** with and without Co(*N*-tpy)$_2^{3+/2+}$ RS.

Co(tpy)$_2^{2+}$ was also evaluated *via* TAS (Table S7) with each of the dyes, and the k_{reg} rates were found to be more than an order of magnitude faster than with Co(*N*-tpy)$_2^{2+}$. The slower kinetics for the halogen-bonding RS, Co(*N*-tpy)$_2^{2+}$, as compared to the nonbinding RS, Co(tpy)$_2^{2+}$, may be due to a preorganization of the dye and the RS resulting from halogen-bonding leading to a geometry that is poor for electron-transfer reactions. Additionally, Co(*N*-tpy)$_2^{2+}$ may also bind to the TiO_2 surface which could limit productive dye−RS interactions.

DSC devices were constructed with the Co(*N*-tpy)$_2^{3+/2+}$ RS system as described in the experimental section. The device performance efficiencies were evaluated via current density−voltage (J−V) curves according to the equation PCE = $(J_{SC} \times V_{OC} \times FF)/I_0$, where PCE is the power conversion efficiency, J_{SC} is the short-circuit current density, V_{OC} is the open-circuit voltage, FF is the fill factor, and I_0 is the incident sun intensity (Table S10 and Figures S45 and S46). Additionally, the DSC devices were studied *via* SMPVT and EIS in the dark to probe electron lifetime and recombination resistances within the DSC device (Figures S47 and S48, Table S11). These techniques have been described elsewhere with added details in Supporting Information.[66,67] Figure 11 summarizes the outcomes of all of these studies with the values scaled relative to the lowest value in the series for a measurement. This allows for the rapid comparison of five parameters on a single bar graph. Interestingly, the DSC device PCE was found to increase as the halide increased in size with **AB7** (iodine-based) having the highest performance. *Via* EIS, recombination resistance for the transfer of electrons for the TiO_2−dye interface to the electrolyte was found to also track halide size with this parasitic reaction having the least resistance in the presence of the iodinated dye. Indiscriminate halogen-bonding of the dye to the oxidized RS near the TiO_2 surface could

https://doi.org/10.1021/acs.jpcc.1c05051
J. Phys. Chem. C 2021, 125, 17647−17659

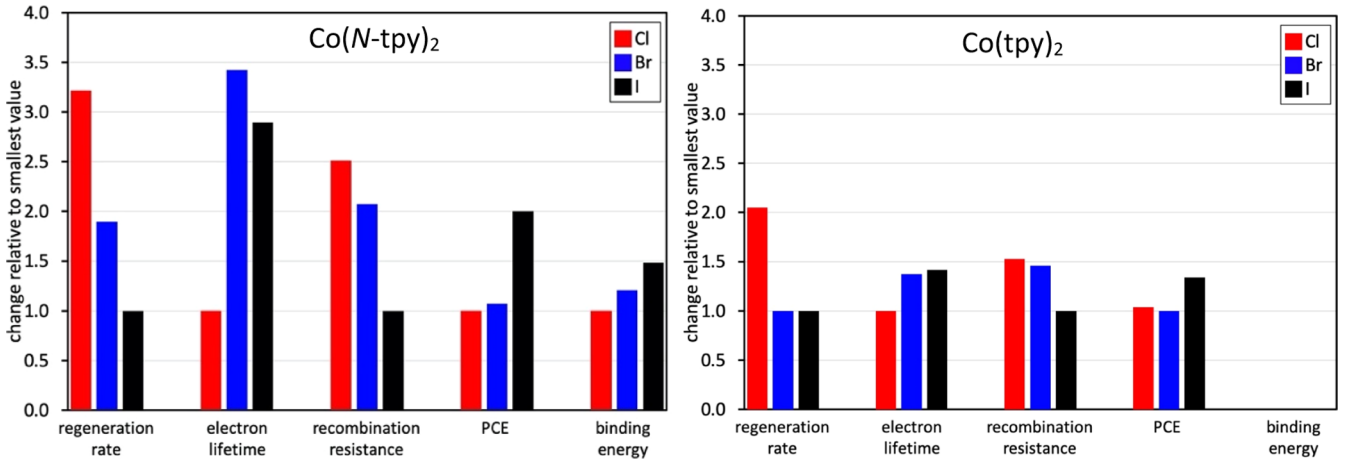

Figure 11. Relative value comparison with each halogenated dye across several interrogation techniques with $Co(N\text{-tpy})_2^{3+/2+}$ (left) and $Co(tpy)_2^{3+/2+}$ (right) as RSs. Note: the binding energy position is left blank for $Co(tpy)_2^{3+/2+}$ since the neutral dyes do not bind the RS at the halide.

Table 4. Comparison of the Changes in Percentages in Each Metric across the Halide Series with $Co(tpy)_2$ and $Co(N\text{-tpy})_2$ as the RS

halide change	RS	J_{sc}	V_{oc}	PCE	EIS	SMPVT
Cl → Br	$Co(tpy)_2$	−3.7%	4.3%	0.2%	−4.7%	33.3%
Cl → Br	$Co(N\text{-tpy})_2$	0%	2.7%	7.1%	−17.5%	200%
Cl → Br	Δ in %	↑3.7%	↓1.6%	↑6.9%	↓−12.8%	↑166.7%
Br → I	$Co(tpy)_2$	28.6%	2.5%	33.9%	−31.4%	8.3%
Br → I	$Co(N\text{-tpy})_2$	76.7%	3.8%	86.7%	−51.8%	−22.2%
Br → I	Δ in %	↑48.1%	↑1.3%	↑52.8%	↓−20.4%	↓−30.5%

possibly be playing a role by increasing the local concentration of the oxidizing RS near the TiO_2 surface.

Interestingly, SMPVT shows long electron lifetimes in TiO_2 that are similar between Br- and I-terminated dyes with the Cl-terminated dye giving DSC devices with much shorter lifetimes. Notably, a minimal difference in electron lifetimes is observed when non-halogen-bonding $Co(tpy)_2^{3+/2+}$ is used (Figures S47). The halogen-binding results track closer to the DSC device performance observations with respect to photovoltage and PCE trends than dark EIS measurements or TAS measurements (Figures S51−S55, Table 4). Computational binding studies show a correlation to device PCE values similar to the SMPVT measurements. Notably, an inverse correlation of binding energy is observed with TAS and EIS measurements. Combined, these results suggest that halogen-bonding increases recombination without increasing the regeneration rate when dark measurements and pulsed illumination techniques are used. It is important to note that the non-steady-state and steady-state illumination experiments do use different electrolyte environments with the full DSC device electrolytes being much more complex. However, a beneficial effect toward device performances is generally observed as the halide on the dye increases in size with steady-state and light intensity-modulated techniques (J−V and SMPVT measurements). This may be related to the need to increase the concentration of the RS under steady-state conditions which is often depleted under continued irradiation.[68] The halogen-bonding approach may enable an increased effective concentration at the dye−TiO_2 interface slowing steady-state depletion.

When $Co(N\text{-tpy})_2$ is compared to the $Co(tpy)_2$ RS system that cannot undergo halogen-bonding, much less dramatic changes are observed for all parameters studied with $Co(tpy)_2$ than $Co(N\text{-tpy})_2$ (Figure 11 and Table 4). Changes across the halide series from Cl-to I-substituted dyes results in 2−3× changes for most parameters with $Co(N\text{-tpy})_2$, while changes are on the order of 1.3−2× when $Co(tpy)_2$ is used. While this could be due to $Co(N\text{-tpy})_2$ being more sensitive to other effects in these studies (*i.e.,* dye loadings, light harvesting, *etc.*) than $Co(tpy)_2$, the finding is also consistent with halogen-bonding occurring due to the larger magnitude of changes. Table 4 compares the percent changes for each parameter when Cl is changed to Br and when Br is changed to I on the dyes for both RSs. Notably, the % change is similar with many parameters between the RSs when Cl- and Br-substituted dyes are compared with only SMPVT showing a large difference. However, upon changing from Br- to I-substituted dyes, the RS performances vary dramatically. While this does not exclude $Co(N\text{-tpy})_2$ from being more sensitive to a particular testing parameter, the similar changes with Cl and Br to the non-halogen-bonding RS and the large difference between Br and I when compared to the non-halogen-bonding RS is consistent with a halogen-bonding effect which would be most pronounced with iodine as the halide.

CONCLUSIONS

Four dyes differing only in the identity of a single atom were synthesized with hydrogen or halogen terminal groups. Steady-state absorption and electrochemical data show favorable energetics and spectral regions where the dye can be selectively photoexcited in the presence of the RSs tested. Computational analysis shows a significant buildup of positive charge at the σ-hole on the halides of the cationic dyes. A halide trend is observed with binding to iodine being 3 kcal/mole stronger

https://doi.org/10.1021/acs.jpcc.1c05051
J. Phys. Chem. C 2021, 125, 17647−17659

than binding to Cl. Interestingly, TAS measurements show that decay of the oxidized dye signal significantly decelerates as the size of the attached halogen atom increases when in the presence of a halogen-binding RS, $Co(N\text{-}tpy)_2^{2+}$. In contrast, the TAS measurements showed significantly less rate change based on halogen effects with the non-halogen-bonding $Co(tpy)_2^{2+/3+}$ RS, as expected. EIS again reveals a negative impact on recombination resistance that can be correlated to halogen-bonding. However, SMPVT and DSC devices show a positive correlation with relation to halogen-bonding events. This suggests that all techniques have correlation to halogen-bonding with dark and pulsed light interrogation techniques showing negative results, but steady-state illumination techniques show a desirable influence consistent with halogen-bonding. We note that these studies do not provide direct evidence of halogen-bonding and only provide data that are consistent with halogen-bonding across several experimental techniques. Notably, these systems are quite complex, and without direct evidence, it is not possible to confirm that halogen-bonding is taking place in these systems since other parameters such as dye absorptivity and dye loadings also change across this series. Future studies are focused on exploring other noncovalent RS−dye interactions within these systems such as those recently highlighted in the literature.[63]

■ ASSOCIATED CONTENT

Supporting Information

The Supporting Information is available free of charge at https://pubs.acs.org/doi/10.1021/acs.jpcc.1c05051.

Characterization data, computational results, nsTAS data, and DSC device data (PDF)

■ AUTHOR INFORMATION

Corresponding Authors

Neeraj Rai − *Dave C. Swalm School of Chemical Engineering and Center for Advanced Vehicular Systems, Mississippi State University, Mississippi State, Mississippi 39762, United States;* orcid.org/0000-0002-0058-9623; Email: neerajrai@che.msstate.edu

Nathan I. Hammer − *Department of Chemistry and Biochemistry, University of Mississippi, University, Mississippi 38677, United States;* orcid.org/0000-0002-6221-2709; Email: nhammer@olemiss.edu

Jared H. Delcamp − *Department of Chemistry and Biochemistry, University of Mississippi, University, Mississippi 38677, United States;* orcid.org/0000-0001-5313-4078; Email: delcamp@olemiss.edu

Authors

Christine Curiac − *Department of Chemistry and Biochemistry, University of Mississippi, University, Mississippi 38677, United States;* orcid.org/0000-0003-2468-8906

Leigh Anna Hunt − *Department of Chemistry and Biochemistry, University of Mississippi, University, Mississippi 38677, United States;* orcid.org/0000-0002-7681-3599

Md Abdus Sabuj − *Dave C. Swalm School of Chemical Engineering and Center for Advanced Vehicular Systems, Mississippi State University, Mississippi State, Mississippi 39762, United States;* orcid.org/0000-0003-1125-5378

Qing Li − *Department of Chemistry and Biochemistry, University of Mississippi, University, Mississippi 38677, United States;* orcid.org/0000-0001-6723-5195

Alexandra Baumann − *Department of Chemistry and Biochemistry, University of Mississippi, University, Mississippi 38677, United States;* orcid.org/0000-0001-7435-5689

Hammad Cheema − *Department of Chemistry and Biochemistry, University of Mississippi, University, Mississippi 38677, United States;* orcid.org/0000-0002-7045-0141

Yanbing Zhang − *Department of Chemistry and Biochemistry, University of Mississippi, University, Mississippi 38677, United States;* orcid.org/0000-0002-8622-0594

Complete contact information is available at: https://pubs.acs.org/10.1021/acs.jpcc.1c05051

Author Contributions

⊥C.C., L.A.H., and M.A.S. contributed equally. The manuscript was written through contributions of all authors. All authors have given approval to the final version of the manuscript.

Notes

The authors declare no competing financial interest.

■ ACKNOWLEDGMENTS

This work was supported by NSF Award OIA-17527220. MAS and NR acknowledge the financial support from the National Science Foundation (OIA-1757220) for the computational aspects of this project. The DFT calculations were performed using supercomputers at the High Performance Computing Collaboratory at Mississippi State University and the Extreme Science and Engineering Discovery Environment (XSEDE), which is supported by the National Science Foundation grant number ACI-1548562. This work used XSEDE Stampede 2 at the Texas Advanced Computing Center (TACC) through allocation TG-CHE140141.

■ ABBREVIATIONS

TiO_2	titanium dioxide
tpy	terpyridine
N-tpy	2,6-di(pyrid-2-yl)pyrazine
CPDT	cyclopentadithiophene
LiTFSI	lithium bis(trifluoromethanesulfonyl)imide
N_2	dinitrogen gas
$NOBF_4$	nitrosonium tetrafluoroborate
RS	redox shuttle
CV	cyclic voltammetry
DFT	density functional theory
nsTAS	nanosecond transient absorption spectroscopy
DS-PECs	dye-sensitized photoelectrochemical cells
CAA	cyanoacrylic acid
ICT	intermolecular charge transfer
CB	conduction band
BET	back electron transfer
SMPVT	small modulated photovoltage transient
EIS	electrochemical impedance spectroscopy
TLC	thin-layer chromatography
NMR	nuclear magnetic resonance
TDDFT	time-dependent density functional theory
SCF	self-consistent field
IEFPCM	integral equation formalism
PCM	polarizable continuum model
DFT	density functional theory
KKW	Kohlrausch−Williams−Watts
CDCA	chenodeoxycholic acid
MOs	molecular orbitals
HOMO	highest occupied molecular orbital

LUMO	lowest unoccupied molecular orbital
CT	charge transfer
SOMO	singly occupied molecular orbital
λ_{max}	absorption maxima
λ_{onset}	absorption curve onset
DCM	dichloromethane
ε	molar absorptivities
MeCN	acetonitrile
NHE	normal hydrogen electrode
MEP	molecular electrostatic potential
VCN	valeronitrile
DSC	dye-sensitized solar cells
PCE	power conversion efficiency
J_{SC}	short-circuit current density
V_{OC}	open-circuit voltage
FF	fill factor
I_0	incident sun intensity
J-V	current density−voltage
ΔOD	change in optical density

REFERENCES

(1) Yu, Z.; Li, F.; Sun, L. Recent advances in dye-sensitized photoelectrochemical cells for solar hydrogen production based on molecular components. *Energy Environ. Sci.* **2015**, *8*, 760−775.

(2) Liu, X.; Inagaki, S.; Gong, J. Heterogeneous Molecular Systems for Photocatalytic CO_2 Reduction with Water Oxidation. *Angew. Chem., Int. Ed.* **2016**, *55*, 14924−14950.

(3) White, J. L.; Baruch, M. F.; Pander, J. E., III; Hu, Y.; Fortmeyer, I. C.; Park, J. E.; Zhang, T.; Liao, K.; Gu, J.; Yan, Y.; Shaw, T. W.; Abelev, E.; Bocarsly, A. B. Light-Driven Heterogeneous Reduction of Carbon Dioxide: Photocatalysts and Photoelectrodes. *Chem. Rev.* **2015**, *115*, 12888−12935.

(4) Luciani, G.; Imparato, C.; Vitiello, G. Photosensitive Hybrid Nanostructured Materials: The Big Challenges for Sunlight Capture. *Catalysts* **2020**, *10*, 103.

(5) Antón-García, D.; Warnan, J.; Reisner, E. A diketopyrrolopyrrole dye-based dyad on a porous TiO2 photoanode for solar-driven water oxidation. *Chem. Sci.* **2020**, *11*, 12769−12776.

(6) Brogdon, P.; Cheema, H.; Delcamp, J. H. Near-Infrared-Absorbing Metal-Free Organic, Porphyrin, and Phthalocyanine Sensitizers for Panchromatic Dye-Sensitized Solar Cells. *ChemSusChem* **2018**, *11*, 86−103.

(7) Saygili, Y.; Stojanovic, M.; Flores-Díaz, N.; Zakeeruddin, S. M.; Vlachopoulos, N.; Grätzel, M.; Hagfeldt, A. Metal Coordination Complexes as Redox Mediators in Regenerative Dye-Sensitized Solar Cells. *Inorganics* **2019**, *7*, 30.

(8) Cole, J. M.; Pepe, G.; Al Bahri, O. K.; Cooper, C. B. Cosensitization in Dye-Sensitized Solar Cells. *Chem. Rev.* **2019**, *119*, 7279−7327.

(9) Ji, J.-M.; Zhou, H.; Kim, H. K. Rational design criteria for D-π-A structured organic and porphyrin sensitizers for highly efficient dye-sensitized solar cells. *J. Mater. Chem. A* **2018**, *6*, 14518−14545.

(10) Wu, Y.; Zhu, W.-H.; Zakeeruddin, S. M.; Grätzel, M. Insight into D-A-π-A Structured Sensitizers: A Promising Route to Highly Efficient and Stable Dye-Sensitized Solar Cells. *ACS Appl. Mater. Interfaces* **2015**, *7*, 9307−9318.

(11) Fakharuddin, A.; Jose, R.; Brown, T. M.; Fabregat-Santiago, F.; Bisquert, J. A perspective on the production of dye-sensitized solar modules. *Energy Environ. Sci.* **2014**, *7*, 3952−3981.

(12) Zhang, S.; Yang, X.; Numata, Y.; Han, L. Highly Efficient Dye-Sensitized Solar Cells: Progress and Future Challenges. *Energy Environ. Sci.* **2013**, *6*, 1443−1464.

(13) Hardin, B. E.; Snaith, H. J.; McGehee, M. D. The renaissance of dye-sensitized solar cells. *Nat. Photonics* **2012**, *6*, 162−169.

(14) Hagfeldt, A.; Boschloo, G.; Sun, L.; Kloo, L.; Pettersson, H. Dye-Sensitized Solar Cells. *Chem. Rev.* **2010**, *110*, 6595−6663.

(15) Schmidt, D.; Hager, M. D.; Schubert, U. S. Photo-Rechargeable Electric Energy Storage Systems. *Adv. Energy Mater.* **2016**, *6*, 1500369.

(16) Friebe, C.; Schubert, U. S. Development of Active Organic and Polymeric Materials for Batteries and Solar Cells: Introduction to Essential Characterization Techniques. *Adv. Energy Mater.* **2015**, *5*, 1500858.

(17) Winsberg, J.; Hagemann, T.; Janoschka, T.; Hager, M. D.; Schubert, U. S. Redox-Flow Batteries: From Metals to Organic Redox-Active Materials. *Angew. Chem., Int. Ed.* **2017**, *56*, 686−711.

(18) Yan, N. F.; Li, G. R.; Gao, X. P. Electroactive Organic Compounds as Anode-Active Materials for Solar Rechargeable Redox Flow Battery in Dual-Phase Electrolytes. *J. Electrochem. Soc.* **2014**, *161*, A736−A741.

(19) Lei, B.; Li, G.-R.; Chen, P.; Gao, X.-P. A Quasi-Solid-State Solar Rechargeable Battery with Polyethylene Oxide Gel Electrolyte. *ACS Appl. Energy Mater.* **2019**, *2*, 1000−1005.

(20) Yu, M.; McCulloch, W. D.; Beauchamp, D. R.; Huang, Z.; Ren, X.; Wu, Y. Aqueous Lithium-Iodine Solar Flow Battery for the Simultaneous Conversion and Storage of Solar Energy. *J. Am. Chem. Soc.* **2015**, *137*, 8332−8335.

(21) Li, W.; Kerr, E.; Goulet, M. A.; Fu, H. C.; Zhao, Y.; Yang, Y.; Veyssal, A.; He, J. H.; Gordon, R. G.; Aziz, M. J.; Jin, S. A Long Lifetime Aqueous Organic Solar Flow Battery. *Adv. Energy Mater.* **2019**, *9*, 1900918.

(22) McCulloch, W. D.; Yu, M.; Wu, Y. pH-Tuning a Solar Redox Flow Battery for Integrated Energy Conversion and Storage. *ACS Energy Lett.* **2016**, *1*, 578−582.

(23) Cavallo, G.; Metrangolo, P.; Milani, R.; Pilati, T.; Priimagi, A.; Resnati, G.; Terraneo, G. The Halogen Bond. *Chem. Rev.* **2016**, *116*, 2478−2601.

(24) Terraneo, G.; Resnati, G.; Metrangolo, P. *Iodine Chemistry and Applications: Chapter 8 Iodine and Halogen Bonding*, 1st ed.; John Wiley & Sons, 2015.

(25) Baumann, A.; Cheema, H.; Sabuj, M. A.; McNamara, L. E.; Zhang, Y.; Peddapuram, A.; Nguyen, S. T.; Watkins, D. L.; Hammer, N. I.; Rai, N.; Delcamp, J. H. Iodine binding with thiophene and furan based dyes for DSCs. *Phys. Chem. Chem. Phys.* **2018**, *20*, 17859−17870.

(26) Hu, K.; Severin, H. A.; Koivisto, B. D.; Robson, K. C. D.; Schott, E.; Arratia-Perez, R.; Meyer, G. J.; Berlinguette, C. P. Direct Spectroscopic Evidence for Constituent Heteroatoms Enhancing Charge Recombination at a TiO_2−Ruthenium Dye Interface. *J. Phys. Chem. C* **2014**, *118*, 17079−17089.

(27) Aghazada, S.; Gao, P.; Yella, A.; Moehl, T.; Teuscher, J.; Moser, J.-E.; Grätzel, M.; Nazeeruddin, M. K. Unravelling the Dual Character of Sulfur Atoms on Sensitizers in the Dye-Sensitized Solar Cells. *ACS Appl. Mater. Interfaces* **2016**, *8*, 26827−26833.

(28) Simon, S. J. C.; Parlane, F. G. L.; Swords, W. B.; Kellett, C. W.; Du, C.; Lam, B.; Dean, R. K.; Hu, K.; Meyer, G. J.; Berlinguette, C. P. Halogen Bonding Promotes Higher Dye-Sensitized Solar Cell Photovoltages. *J. Am. Chem. Soc.* **2016**, *138*, 10406−10409.

(29) Swords, W. B.; Simon, S. J. C.; Parlane, F. G. L.; Dean, R. K.; Kellett, C. W.; Hu, K.; Meyer, G. J.; Berlinguette, C. P. Evidence for Interfacial Halogen Bonding. *Angew. Chem., Int. Ed.* **2016**, *55*, 5956−5960.

(30) Parlane, F. G. L.; Mustoe, C.; Kellett, C. W.; Simon, S. J.; Swords, W. B.; Meyer, G. J.; Kennepohl, P.; Berlinguette, C. P. Spectroscopic detection of halogen bonding resolves dye regeneration in the dye-sensitized solar cell. *Nat. Commun.* **2017**, *8*, 1761.

(31) Nguyen, T.-D.; Lin, C.-H.; Wu, C.-G. Effect of the CF_3 Substituents on the Charge-Transfer Kinetics of High-Efficiency Cyclometalated Ruthenium Sensitizers. *Inorg. Chem.* **2017**, *56*, 252−260.

(32) Casarin, L.; Swords, W. B.; Caramori, S.; Bignozzi, C. A.; Meyer, G. J. Rapid Static Sensitizer Regeneration Enabled by Ion Pairing. *Inorg. Chem.* **2017**, *56*, 7324−7327.

(33) Ogunsolu, O. O.; Braun, A. J.; Robb, A. J.; Salpage, S. R.; Zhou, Y.; Hanson, K. Influence of Dye-Coordinated Metal Ions on Electron

https://doi.org/10.1021/acs.jpcc.1c05051
J. Phys. Chem. C 2021, 125, 17647−17659

Transfer Dynamics at Dye−Semiconductor Interfaces. *ACS Appl. Energy Mater.* **2018**, *2*, 29−36.
(34) Hu, Y.; Abate, A.; Cao, Y.; Ivaturi, A.; Zakeeruddin, S. M.; Grätzel, M.; Robertson, N. High Absorption Coefficient Cyclopentadithiophene Donor-Free Dyes for Liquid and Solid-State Dye-Sensitized Solar Cells. *J. Phys. Chem. C* **2016**, *120*, 15027−15034.
(35) Wiberg, J.; Marinado, T.; Hagberg, D. P.; Sun, L.; Hagfeldt, A.; Albinsson, B. Effect of Anchoring Group on Electron Injection and Recombination Dynamics in Organic Dye-Sensitized Solar Cells. *J. Phys. Chem. C* **2009**, *113*, 3881−3886.
(36) Zhang, L.; Cole, J. M. Anchoring groups for dye-sensitized solar cells. *ACS Appl. Mater. Interfaces* **2015**, *7*, 3427−3455.
(37) Delcamp, J. H.; Yella, A.; Holcombe, T. W.; Nazeeruddin, M. K.; Grätzel, M. The molecular engineering of organic sensitizers for solar-cell applications. *Angew. Chem., Int. Ed.* **2013**, *52*, 376−380.
(38) Nguyen, S. T.; Rheingold, A. L.; Tschumper, G. S.; Watkins, D. L. Elucidating the Effects of Fluoro and Nitro Substituents on Halogen Bond Driven Assemblies of Pyridyl-Capped π-Conjugated Molecules. *Cryst. Growth Des.* **2016**, *16*, 6648−6653.
(39) Connelly, N. G.; Geiger, W. E. Chemical Redox Agents for Organometallic Chemistry. *Chem. Rev.* **1996**, *96*, 877−910.
(40) Foltz, R. D. *Handbook of Physics and Chemistry*, 63rd ed.; CRC: Boca Raton, FL, 1982.
(41) Karsten, B. P.; Bijleveld, J. C.; Viani, L.; Cornil, J.; Gierschner, J.; Janssen, R. A. J. Electronic structure of small band gap oligomers based on cyclopentadithiophenes and acceptor units. *J. Mater. Chem.* **2009**, *19*, 5343−5350.
(42) Guo, S.; Yan, W.; Chen, J.; Tang, C.; Wang, Z.; Jiang, J.; Xin, H. Synthesis of star-shaped non-fullerene acceptors and their applications in organic solar cells. *Synth. Met.* **2018**, *245*, 167−174.
(43) Tsao, H. N.; Grätzel, M. Illumination Time Dependent Learning in Dye Sensitized Solar Cells. *ACS Appl. Mater. Interfaces* **2018**, *10*, 36602−36607.
(44) Kershaw Cook, L. J.; Tuna, F.; Halcrow, M. A. Iron(II) and cobalt(II) complexes of tris-azinyl analogues of 2,2':6',2''-terpyridine. *Dalton Trans.* **2013**, *42*, 2254−2265.
(45) Frisch, M. J.; Trucks, G. W.; Schlegel, H. B.; Scuseria, G. E.; Robb, M. A.; Cheeseman, J. R.; Scalmani, G.; Barone, V.; Petersson, G. A.; Nakatsuji, H.; Li, X.; Caricato, M.; Marenich, A. V.; Bloino, J.; Janesko, B. G.; Gomperts, R.; Mennucci, B.; Hratchian, H. P.; Ortiz, J. V.; Izmaylov, A. F.; Sonnenberg, J. L.; Williams-Young, D.; Ding, F.; Lipparini, F.; Egidi, F.; Goings, J.; Peng, B.; Petrone, A.; Henderson, T.; Ranasinghe, D.; Zakrzewski, V. G.; Gao, J.; Rega, N.; Zheng, G.; Liang, W.; Hada, M.; Ehara, M.; Toyota, K.; Fukuda, R.; Hasegawa, J.; Ishida, M.; Nakajima, T.; Honda, Y.; Kitao, O.; Nakai, H.; Vreven, T.; Throssell, K.; Montgomery, J. A., Jr.; Peralta, J. E.; Ogliaro, F.; Bearpark, M. J.; Heyd, J. J.; Brothers, E. N.; Kudin, K. N.; Staroverov, V. N.; Keith, T. A.; Kobayashi, R.; Normand, J.; Raghavachari, K.; Rendell, A. P.; Burant, J. C.; Iyengar, S. S.; Tomasi, J.; Cossi, M.; Millam, J. M.; Klene, M.; Adamo, C.; Cammi, R.; Ochterski, J. W.; Martin, R. L.; Morokuma, K.; Farkas, O.; Foresman, J. B.; Fox, D. J. *Gaussian 16*, Revision A.03; Gaussian, Inc.: Wallingford CT, 2016.
(46) Chai, J.-D.; Head-Gordon, M. Long-range corrected hybrid density functionals with damped atom-atom dispersion corrections. *Phys. Chem. Chem. Phys.* **2008**, *10*, 6615−6620.
(47) Grimme, S. Semiempirical GGA-type density functional constructed with a long-range dispersion correction. *J. Comput. Chem.* **2006**, *27*, 1787−1799.
(48) Feller, D. The Role of Databases in Support of Computational Chemistry Calculations. *J. Comput. Chem.* **1996**, *17*, 1571−1586.
(49) Schuchardt, K. L.; Didier, B. T.; Elsethagen, T.; Sun, L.; Gurumoorthi, V.; Chase, J.; Li, J.; Windus, T. L. Basis Set Exchange: A Community Database for Computational Sciences. *J. Chem. Inf. Model.* **2007**, *47*, 1045−1052.
(50) Francl, M. M.; Pietro, W. J.; Hehre, W. J.; Binkley, J. S.; Gordon, M. S.; DeFrees, D. J.; Pople, J. A. Self-consistent molecular orbital methods. XXIII. A polarization-type basis set for second-row elements. *J. Chem. Phys.* **1982**, *77*, 3654−3665.
(51) Bacskay, G. B. A quadratically convergent Hartree-Fock (QC-SCF) method. Application to closed shell systems. *Chem. Phys.* **1981**, *61*, 385−404.
(52) Tomasi, J.; Mennucci, B.; Cammi, R. Quantum Mechanical Continuum Solvation Models. *Chem. Rev.* **2005**, *105*, 2999−3094.
(53) Miertuš, S.; Scrocco, E.; Tomasi, J. Electrostatic Interactions of a Solute with a Continuum. A Direct Utilization of Ab Initio Molecular Potentials for the Prevision of Solvent Effects. *Chem. Phys.* **1981**, *55*, 117−129.
(54) Cossi, M.; Barone, V.; Cammi, R.; Tomasi, J. Ab initio study of solvated molecules: A new implementation of the polarizable continuum model. *Chem. Phys. Lett.* **1996**, *255*, 327−335.
(55) Foresman, J. B.; Frisch, A. *Exploring Chemistry with Electronic Structure Methods: A Guide to Using Gaussian*, 2nd ed.; Gaussian, Inc.: Pittsburgh, PA, 2013.
(56) Adamo, C.; Jacquemin, D. The calculations of excited-state properties with Time-Dependent Density Functional Theory. *Chem. Soc. Rev.* **2013**, *42*, 845−856.
(57) Bauernschmitt, R.; Ahlrichs, R. Treatment of electronic excitations within the adiabatic approximation of time dependent density functional theory. *Chem. Phys. Lett.* **1996**, *256*, 454−464.
(58) Kohlrausch, R. Theorie des elektrischen Rückstandes in der Leidener Flasche. *Ann. Phys.* **1854**, *167*, 179−214.
(59) Williams, G.; Watts, D. C. Non-Symmetrical Dielectric Relaxation Behaviour Arising from a Simple Empirical Decay Function. *Trans. Faraday Soc.* **1970**, *66*, 80−85.
(60) Lindsey, C. P.; Patterson, G. D. Detailed comparison of the Williams−Watts and Cole−Davidson functions. *J. Chem. Phys.* **1980**, *73*, 3348−3357.
(61) Lukichev, A. Physical meaning of the stretched exponential Kohlrausch function. *Phys. Lett. A* **2019**, *383*, 2983−2987.
(62) Li, F.; Jennings, J. R.; Wang, Q. Determination of sensitizer regeneration efficiency in dye-sensitized solar cells. *ACS Nano* **2013**, *7*, 8233−8242.
(63) Cho, I.; Wagner, P.; Innis, P. C.; Mori, S.; Mozer, A. J. Substrate-Dependent Electron-Transfer Rate of Mixed-Ligand Electrolytes: Tuning Electron-Transfer Rate without Changing Driving Force. *J. Am. Chem. Soc.* **2021**, *143*, 488−495.
(64) Yang, J.; Ganesan, P.; Teuscher, J.; Moehl, T.; Kim, Y. J.; Yi, C.; Comte, P.; Pei, K.; Holcombe, T. W.; Nazeeruddin, M. K.; Hua, J.; Zakeeruddin, S. M.; Tian, H.; Grätzel, M. Influence of the Donor Size in D-pi-A Organic Dyes for Dye-Sensitized Solar Cells. *J. Am. Chem. Soc.* **2014**, *136*, 5722−5730.
(65) Wallace, A. M.; Curiac, C.; Delcamp, J. H.; Fortenberry, R. C. Accurate determination of the onset wavelength (λ_{onset}) in optical spectroscopy. *J. Quant. Spectrosc. Radiat. Transfer* **2021**, *265*, 107544.
(66) Boschloo, G.; Häggman, L.; Hagfeldt, A. Quantification of the Effect of 4-tert-Butylpyridine Addition to I^-/I_3^- Redox Electrolytes in Dye-Sensitized Nanostructured TiO_2 Solar Cells. *J. Phys. Chem. B* **2006**, *110*, 13144−13150.
(67) Wang, Q.; Moser, J.-E.; Grätzel, M. Electrochemical Impedance Spectroscopic Analysis of Dye-Sensitized Solar Cells. *J. Phys. Chem. B* **2005**, *109*, 14945−14953.
(68) Houle, F. A. Adaptive response by an electrolyte: resilience to electron losses in a dye-sensitized porous photoanode. *Chem. Sci.* **2021**, *12*, 6117−6128.

https://doi.org/10.1021/acs.jpcc.1c05051
J. Phys. Chem. C 2021, 125, 17647−17659